Near-Surface Temperature Inversion Growth Rate during the Onset of the Stable Boundary Layer

Ivo G. S. van Hooijdonk, Herman J. H. Clercx, Carsten Abraham, Amber M. Holdsworth, Adam H. Monahan, Etienne Vignon, Arnold F. Moene, Peter Baas, and Bas J. H. van de Wiel

October 2017

Near-Surface Temperature Inversion Growth Rate during the Onset of the Stable Boundary Layer

IVO G. S. VAN HOOIJDONK AND HERMAN J. H. CLERCX

Fluid Dynamics Laboratory, and J. M. Burgerscentrum, Eindhoven University of Technology, Eindhoven, Netherlands

CARSTEN ABRAHAM, AMBER M. HOLDSWORTH, AND ADAM H. MONAHAN

School of Earth and Ocean Sciences, University of Victoria, Victoria, British Columbia, Canada

ETIENNE VIGNON

IGE, Grenoble Alps University/CNRS/IRD, Grenoble, France

ARNOLD F. MOENE

Meteorology and Air Quality Group, Wageningen University and Research, Wageningen, Netherlands

PETER BAAS AND BAS J. H. VAN DE WIEL

Faculty of Civil Engineering and Geosciences, Department of Geoscience and Remote Sensing, Delft University of Technology, Delft, Netherlands

(Manuscript received 15 March 2017, in final form 17 July 2017)

ABSTRACT

This study aims to find the typical growth rate of the temperature inversion during the onset of the stable boundary layer around sunset. The sunset transition is a very challenging period for numerical weather prediction, since neither accepted theories for the convective boundary layer nor those for the stable boundary layer appear to be applicable. To gain more insight in this period, a systematic investigation of the temperature inversion growth rate is conducted. A statistical procedure is used to analyze almost 16 years of observations from the Cabauw observational tower, supported by observations from two additional sites (Dome C and Karlsruhe). The results show that, on average, the growth rate of the temperature inversion (normalized by the maximum inversion during the night) weakly declines with increasing wind speed. The observed growth rate is quantitatively consistent among the sites, and it appears insensitive to various other parameters. The results were also insensitive to the afternoon decay rate of the net radiation except when this decay rate was very weak. These observations are compared to numerical solutions of three models with increasing complexity: a bulk model, an idealized single-column model (SCM), and an operational-level SCM. It appears only the latter could reproduce qualitative features of the observations using a first-order closure. Moreover, replacing this closure with a prognostic TKE scheme substantially improved the quantitative performance. This suggests that idealized models assuming instantaneous equilibrium flux-profile relations may not aid in understanding this period, since history effects may qualitatively affect the dynamics.

1. Introduction

During the sunset transition the incoming shortwave radiation from the sun gradually lessens. As a result, the convective boundary layer (CBL) weakens and a temperature inversion starts to form near the surface, which is the onset of the stable boundary layer (SBL). Typically, the temperature inversion grows within a few hours and then remains relatively constant until sunrise. It is the early growth that we are interested in for

Denotes content that is immediately available upon publication as open access.

Corresponding author: Ivo G. S. van Hooijdonk, i.g.s.v.hooijdonk@tue.nl

DOI: 10.1175/JAS-D-17-0084.1

this study. In particular, we use both observations and numerical models to investigate what parameters determine how fast the SBL evolves during this period.

During the late afternoon, turbulence in the boundary layer is typically decaying (Stull 2000). Much research effort has been aimed at understanding this period on the full range from fundamental studies (van Heerwaarden and Mellado 2016), to practical models (Nadeau et al. 2011), and observations (Blay-Carreras et al. 2014; Jensen et al. 2016). The same is true for the established SBL (Armenio and Sarkar 2002; Sorbjan 2010; Ansorge and Mellado 2016; Mahrt 2014; van Hooijdonk et al. 2017).

These previous studies of the SBL have mostly relied on Monin–Obukhov similarity theory (MOST; Monin 1970), which, once the SBL is established, provides a reasonable description for a broad range of conditions (Sorbjan 2010; Grachev et al. 2013). The decaying turbulence itself, before the onset of the SBL, may also exhibit self-similar behavior, at least for strongly convective situations with weak synoptic forcing (e.g., Nadeau et al. 2011; van Heerwaarden and Mellado 2016). Thus, our understanding of both the (quasi) steady CBL and the (quasi) steady SBL has progressed significantly, despite their own challenges (Holtslag et al. 2013; Lothon et al. 2014).

This understanding and resulting parameterizations may be of limited use during the sunset transition itself (e.g., Sun et al. 2003), since the onset of the SBL typically occurs a few hours before the net radiation becomes negative (van der Linden et al. 2017). Consequently, the decay of convective turbulence and the SBL coexist and interact during the sunset transition (Nadeau et al. 2011; Blay-Carreras et al. 2014). This period is therefore very challenging for numerical weather prediction models (Lothon et al. 2014). Moreover, large-eddy simulation is complicated owing to the changing resolution and domain requirements during the transition (Basu et al. 2008) and the importance of other processes, such as radiative transfer (Edwards 2009). Therefore, it is very important to gain observationally based insight into the period just after the onset of the SBL. As an initial step, we investigate the evolution of the temperature inversion for a broad range of conditions.

Most studies that have focused on the near-surface temperature (inversion) in the SBL have related the instantaneous temperature inversion to other flow variables (André and Mahrt 1982; Sorbjan 2006; Vignon et al. 2017), on detailed investigation of individual cases (Sun et al. 2003), or on mechanistic understanding of the "steady state" (van de Wiel et al. 2012; van Hooijdonk et al. 2015; van de Wiel et al. 2017). However, the temporal behavior starting at the onset of the SBL has received relatively little attention.

A few studies have explicitly aimed at the temporal evolution of the temperature during this period. Earlier work often assumed a square root dependence of the inversion strength with time (e.g., Stull 1983). Whiteman et al. (2004) studied the onset of the SBL within sinkholes, as measured by the evolution of the temperature inversion. Since the wind was always weak inside the sinkholes, the evolution could be modeled considering radiative processes only, and hence the sky-view factor was identified as a key parameter for the temporal evolution inside the sinkholes. A follow-up study by De Wekker and Whiteman (2006) extended to plains and basins, using an exponentially decaying function to fit the time series of the absolute temperature to determine a "typical" time scale during clear and calm nights.

Another study by Pattantyús-Ábrahám and Jánosi (2004) also studied the absolute temperature evolution during 2 years at two distinct sites. They specifically limited their analysis to cases where an exponential fit provided excellent agreement with the time series, which again mostly corresponded to clear and calm nights with wind speed less than $2\,\mathrm{m\,s^{-1}}$. Despite the large number of (predominantly moisture- and radiation-related) quantities they investigated, no clear relation of the time scale was found with any of these. Edwards (2009) used an idealized single-column model (SCM) to study the early evolution of the SBL at weak winds. His main focus was the importance of radiative processes on the near-surface heat budget, while the time scales of the boundary layer evolution did not receive attention. Later, Edwards (2011) imposed the tendency of the surface temperature in a dimensionless model to study the evolution of the sensible heat flux. Nieuwstadt and Tennekes (1981) used a similar imposed tendency to model the evolution of the boundary layer height.

We employ a similar approach to De Wekker and Whiteman (2006) in the sense that a typical time scale is determined for each night. In our case this time scale is based on the growth of the temperature inversion rather than the decay of the absolute temperature. Therefore, we use a logistic growth function, instead of an exponential function, to fit the time series of the temperature inversion (see section 2). Realizing that our approach is heuristic, the typical time scale is considered to be representative of the rate at which the SBL evolves.

The main analysis focuses on a large number of observations from the Cabauw Experimental Site for Atmospheric Research (CESAR) observatory (the Netherlands). These are supported by observations from the Karlsruhe station (Germany) and the Dome C

observatory (Antarctica). The Cabauw and Dome C sites are essentially flat, and the Karlsruhe site is located in a small forest clearing in a wide valley. To aid the interpretation, we use three types of numerical simulations: a bulk model for the SBL, which is based on van de Wiel et al. (2017); a single-column model for the SBL (A. M. Holdsworth and A. H. Monahan 2017, unpublished manuscript); and the Regional Atmospheric Climate Model (RACMO)-SBL, the single-column version of an operational-level regional climate model of the Royal Dutch Meteorological Institute (Baas et al. 2017, manuscript submitted to *Bound.-Layer Meteor.*).

This analysis is used to answer the following questions: To what physical quantities is the rate at which the SBL evolves during the hours around sunset most sensitive? How may this (in)sensitivity be explained? And how similar are the results for three contrasting sites? A major part of the analysis is dedicated specifically to the wind speed dependence, since this quantity has been identified as a key parameter for the characterization of the SBL (Sun et al. 2012; van Hooijdonk et al. 2015; Monahan et al. 2015; Acevedo et al. 2016; van de Wiel et al. 2017).

This paper is organized as follows. In section 2 the important meteorological quantities in this study, the observations sites, and the numerical methods are discussed. Section 3 contains the results, which are then discussed in section 4. The paper is concluded in section 5.

2. Methods

a. Parameter definition

We investigate the temporal evolution of the near-surface temperature inversion $\Delta\theta = \theta(z_2) - \theta(z_1)$, where $\theta(z)$ is the potential temperature at height z (and $z_2 > z_1$). For each night we obtain a characteristic temperature evolution rate of $\Delta\theta$, which we denote $\partial_t\Delta\theta$. In this section, we introduce how $\partial_t\Delta\theta$ is determined, followed by several key parameters that may affect $\partial_t\Delta\theta$.

First, time is defined relative to the time the net radiation Q_N becomes negative; that is, we define sunset at $t = 0$ when $Q_N = 0$ [see also van Hooijdonk et al. (2015)]. Typically this occurred several hours before the meteorological sunset, and 1–2 h after the onset of the SBL (cf. van der Linden et al. 2017).

To define $\partial_t\Delta\theta$, a logistic growth function was used to fit the time series of $\Delta\theta$ (Fig. 1a; details in the appendix). Previously, an exponential function was used by De Wekker and Whiteman (2006) to fit the time series of the cumulative (vertically integrated) cooling. For the temperature inversion we found the logistic growth more suitable, since it captures both the initial and the "final" stage of inversion growth with reasonable accuracy owing to the inflection point. Moreover, the logistic growth was more robust to variations in the interval on which the fit was based.

The logistic growth function is defined as

$$f(t) = \frac{T}{1 + \exp[-k(t - t_0)]}, \tag{1}$$

where T, k, and t_0 are parameters to be estimated: T represents the estimated maximum of the temperature inversion, k is the steepness of the curve, and t_0 is the time at which the inflection point occurs. We define the typical evolution of $\Delta\theta$ as

$$\partial_t\Delta\theta \equiv \frac{Tk}{4}, \tag{2}$$

which is the derivative of f at the inflection point at $t = t_0$.

Additionally, a temperature scale $\Delta\theta_{\max}$ is defined as the maximum temperature inversion (based on 10-min averages) during each night. Using 30-min averages instead did not have a large impact (typically $\lesssim$3% decrease). To reduce the effect of synoptic changes during the night, the detection of the maximum was limited to $t < 5$ h and to 0000 LST at Cabauw and Karlsruhe, respectively. For most nights this had no effect on the value of $\Delta\theta_{\max}$, since the maximum inversion typically occurs early in a night at these locations, probably because pressure acceleration may slightly reduce the inversion strength at later times. At the Dome C the evolution is more gradual and less prone to synoptic variability (Vignon et al. 2017). Therefore, no time restriction was imposed for this site. The temperature scale is used to normalize $\partial_t\Delta\theta$, which results in the inverse time scale $\Delta\theta_{\max}^{-1}\partial_t\Delta\theta$. Alternatively T could be used as a temperature scale. However, we found that measuring $\Delta\theta_{\max}$ directly was more robust.

The quality of the fit greatly varied between nights owing to irregular time series. Therefore, we defined a measure for the quality of the fit, denoted by η^2, which is the mean-squared residual with respect to the observations normalized by $\Delta\theta_{\max}$. Only nights in which $\eta^2 < 0.02$ were used for the analysis (see Table 1). This value is an arbitrary trade-off between the fit quality and the quantity of the nights used for the analysis. Regular checks showed that the results were largely insensitive to the precise value of the threshold, with one caveat. During nights with clouds, the time series of the observations were typically more irregular, which affected the fit quality. Therefore, the selection on η^2 resulted in a

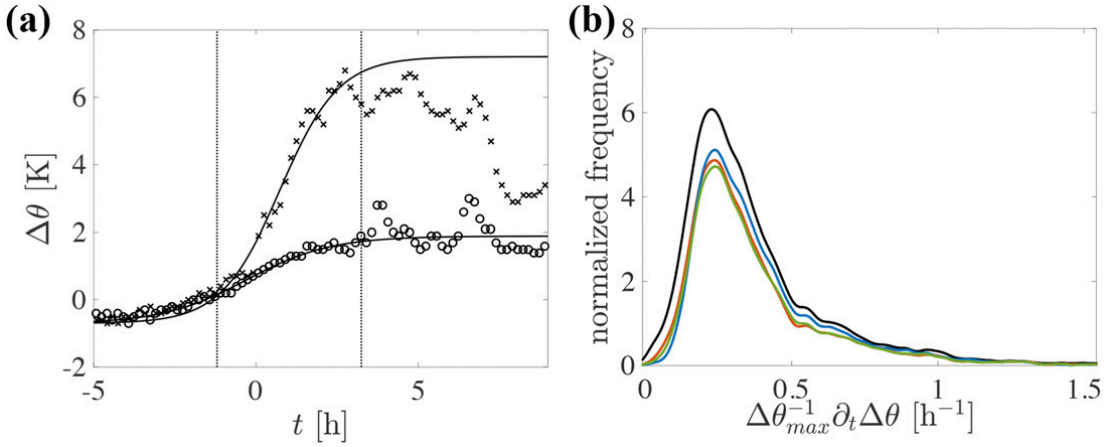

FIG. 1. (a) Time series of the temperature inversion between 40 and 1.5 m for two example cases at Cabauw: 24 Aug (crosses) and 29 Aug 2001 (circles). Solid lines are examples of a fit through the observations using Eq. (1). The vertical dotted lines indicate the approximate time interval on which the fitting procedure was based. (b) The normalized frequency of $\Delta\theta_{\max}^{-1}\partial_t\Delta\theta$ at Cabauw for all nights (black) and all nights for which $\eta^2 < 0.02$ (blue). The other lines show that a similar frequency distribution may be obtained when the selection was based on cloud-related parameters (both are defined in the main text), instead of selection on fit quality η^2. The lines represent all nights for which $\partial_t Q_N < -20$ W m^{-2} h^{-1} (red) and all nights for which $Q_{N,\min} < -35$ W m^{-2} (green).

sampling bias, since a relatively large fraction of the cloudy cases were affected compared to clear-sky cases (Fig. 1b). Similarly, the selection on η^2 introduced a minor bias toward lower relative humidity, larger (negative) net radiation, and a slightly weaker wind speed. However, the remaining set of nights in the present study still spans a much broader range of conditions than the stringent selection of Pattantyús-Ábrahám and Jánosi (2004).

Since wind speed has been identified as a key parameter for the SBL (Sun et al. 2012; van de Wiel et al. 2012), we characterize each night by the mean wind speed around (the net-radiation based) sunset U_{sunset}. At this time the wind speed has a strong vertical correlation, and thus the wind speed at a single altitude may be used as a measure for the mechanical forcing. In each case the highest level on which $\Delta\theta$ was based was used to obtain U_{sunset}. As an averaging period we chose the interval $t \in [-2, 1]$ h. We investigated the sensitivity to this choice by arbitrarily choosing different averaging periods within the time range $t \in [-4, 1]$ h. Between these choices the resulting values of U_{sunset} were strongly correlated (not shown), indicating insensitivity to the particular choice.

The established SBL may be characterized further using the net radiative emission Q_N (defined positive toward the surface). Several hours after sunset the net radiation minimizes (maximizes in absolute sense) and remains relatively constant. This minimum value $Q_{N,\min}$ was used as a characteristic measure. Since Q_N evolves during the sunset transition itself, we also define $\partial_t Q_N$ as the decay rate of Q_N. Using a similar procedure as for $\partial_t\Delta\theta$, $\partial_t Q_N$ was determined based on a linear fit to the time series of Q_N (details are in the

TABLE 1. The characteristic values of the quantities introduced in section 2a. For each quantity listed in the first column, the minimum (min) and maximum (max) values, the mean μ, and standard deviation σ are listed as an indication of the observational spread of each quantity for each site. The final row contains the number of nights that had sufficient data and fit quality to be used in the analysis and two fractions (f_1, f_2); f_1 indicates how many nights could be used as fraction of the total number of nights, and f_2 indicates a similar fraction relative to the number of nights that had sufficient quality of the data (e.g., preselected on missing data points).

	Cabauw				Dome C				Karlsruhe			
	Min	Max	μ	σ	Min	Max	μ	σ	Min	Max	μ	σ
U_{sunset} (m s^{-1})	0.6	18.9	5.5	2.5	0.5	11.4	4.2	1.6	0.0	11.1	3.5	1.5
$\Delta\theta_{\max}$ (K)	0.3	9.2	2.6	1.5	2.3	20.6	8.7	3.7	0.7	9.4	4.5	1.7
$Q_{N,\min}$ (W m^{-2})	−99	0.0	−48	18	−75	−26	−46	7.0	—	—	—	—
$\partial_t\Delta\theta$ (K h^{-1})	0.0	11	0.8	0.6	0.3	7.3	1.7	0.9	0.2	4.7	1.5	0.7
$\partial_t Q_N$ (W m^{-2} h^{-1})	−114	2.8	−47	25	−17	−8.2	−13	1.6	—	—	—	—
Nights (f_1, f_2)	3928 (0.72, 0.73)				106 (0.16, 0.95)				2524 (0.46, 0.68)			

appendix). A linear decrease provided a reasonable representation of the time series between several hours before sunset until shortly after sunset. Moreover, we did not find significant improvement when a more elaborate fit function (e.g., a sine function) was used. The slope of the linear fit provides an estimate of $\partial_t Q_N$. The ratio $Q_{N,\min}^{-1}\partial_t Q_N$ defines an inverse time scale characterizing how fast Q_N evolves toward its steady state.

Because of the differences in the relative importance of radiative, turbulent, and soil heat fluxes in the two regimes, it is possible that the character of the growth of the inversion may differ fundamentally in the very stable boundary layer (VSBL) from that in the weakly stable boundary layer (WSBL). As such, we will investigate the growth of the inversion separately in these two regimes. To separate the two regimes in observations, we make use of a hidden Markov model (HMM) analysis [as in Monahan et al. (2015), who also provided an introductory example for this method]. This approach models the observed variable x_i, $i = 1, \ldots, N$, as being dependent on an unobserved Markov chain z_i taking a set of K discrete values (the so-called hidden states). At each time, the HMM associates the observation with one of a number (in our case, 2) of probability distributions, resulting in a time series of HMM states. More technically, conditioned on z_i residing in state k, the distribution of x_i is described by a specified probability density function $p(x_i, \lambda_k)$ (where λ_k, $k = 1, \ldots, K$, is a state-dependent set of parameters). For a specified number K of hidden states, the HMM algorithm finds maximum likelihood estimates both of the parameters λ_k and the hidden state trajectory z_i. Having obtained this discrete hidden-state trajectory, conditional probability distributions of any observations concurrent with those used in the HMM can be estimated.

A benefit of the HMM approach is that the separation of states is determined by the intrinsic structure of the data, rather than relying on subjective thresholds (which may be impossible to define in high-dimensional datasets). In this study, we follow the approach of Monahan et al. (2015), distinguishing the VSBL and the WSBL using a two-state HMM applied to three-dimensional data from Cabauw (the wind speed at 10 and 200 m and the potential temperature difference between 2 and 200 m, all at 10-min resolution).

b. *Observation sites*

Data from three observational sites were used for this study. The main focus lies on the CESAR observatory, while the Karlsruhe and Dome C stations are used to verify consistency of results among sites. To provide insight in the climate of each site, several characteristic values of the quantities introduced in the previous section are listed in Table 1.

The CESAR observatory near Cabauw, the Netherlands (51.971°N, 4.927°E), and its surroundings are extensively described in van Ulden and Wieringa (1996). Further details on the measurement equipment and the tower configuration may be found at http://www.cesar-observatory.nl. The surface is mostly covered with short grass and the surrounding land is relatively flat. We use observations collected between January 2001 and October 2016. The wind speed and direction (cup anemometers) and the (potential) temperature (KNMI Pt500 Element) are measured at 10, 20, 40, 80, 140, and 200 m. Additionally, the temperature is measured at 1.5 (all years) and 0.1 m (since 2013). The relative humidity is derived from the air and dewpoint temperature (Vaisala HMP243) at 1.5 m. All measurements are based on 10-min averages. The net radiation Q_N is composed of the longwave and shortwave incoming and outgoing radiation components measured at 1 m. Measurements of the cloud cover have been obtained using a nubiscope (Wauben et al. 2010) since 2008. More or less continuous cloud-cover measurements are available since mid-2009.

The Karlsruhe Boundary Layer Measurement Tower (49.176°N, 8.425°E) is located in the eastern Rhine Valley. We use the observations of the temperature (Pt-100) at 2, 30, 60, and 100 m, and of the wind speed (cup anemometers) at 30, 60, and 100 m (all based on 10-min averages). The observational period is January 2001–December 2016. The valley is about 30 km wide and hills of about 250 m are found 10 km to the east. Larger hills are approximately 50 km to the east and north. The tower is placed in a small forest clearing, a distance of 10–25 m in each direction from the tree line. The canopy height of the forest is 30 m. Further details on the site and the instrumentation may be found in Kalthoff and Vogel (1992) and at http://imkbemu.physik.uni-karlsruhe.de/~fzkmast/. To the northeast the urbanized area of the Karlsruhe Institut für Technologie is located, with buildings higher than 30 m at about 200 m from the tower. Since the forest affects the radiation measurements during sunset and sunrise (M. Kohler 2017, personal communication), these data were not used in our analysis. The sunset was therefore estimated based on the temperature inversion. For our analysis at this site the exact time of sunset is not important.

The Dome C observatory is located on Antarctica (75.06°S, 123.200°E). The station is located on a continental-scale dome (3233 m AGL), and the local

slope is very weak (<1%). We use 30-min averages of the temperature (Campbell HMP155 thermohygrometers in mechanically ventilated shields) and the wind measurements (Young 05106 aerovanes) from a 45-m tower at $z = [18, 25, 33, 41]$ m. Additionally, the surface skin temperature is estimated from longwave radiation measurements. Detailed information on the instrumentation and processing are given by Genthon et al. (2013) and Vignon et al. (2016) (see also http://www.institut-polaire.fr/ipev-en/infrastructures-2/stations/concordia/). The analysis is limited to nights with a clear diurnal cycle in the months November–February during the period November 2011–December 2016 (i.e., the Antarctic summer). During the Antarctic summer the sun never sets; that is, the shortwave incoming radiation is always nonzero. Nonetheless, the net radiation does become negative during the ''night'' owing to variations in the zenith angle. It should be noted that the diurnal cycle of Q_N is much weaker than at Cabauw, owing to the lower zenith angle and the higher surface albedo.

c. Numerical models

This section provides an overview of the three numerical models that were used to aid the interpretation of the observations. These models have been described elsewhere, and our main interest is to what extent each model reproduces elements of the observations. As such, only a brief summary of each model is given here, and we do not discuss the merits and drawbacks of specific model choices. For detailed descriptions of the models, the reader is referred to the cited papers.

The bulk model is used with the aim to obtain rudimentary understanding of the SBL dynamics. The model is based on the idealized model by van de Wiel et al. (2017), and it uses a single evolution equation for the temperature inversion:

$$\partial_t \Delta\theta(t|z_{\rm ref}) = \frac{|Q_N(t)|}{c_v} - \frac{A}{c_v}\Delta\theta(t|z_{\rm ref}) f(R_b), \qquad (3)$$

where $\Delta\theta$ is the time-dependent temperature difference between the surface and a constant air temperature at reference height $z_{\rm ref}$, c_v is the heat capacity of the surface per square meter, and a proportionality constant $A = \rho c_p c_D U$, in which ρ is the density of air, c_p is the specific heat capacity of air at constant pressure, and U is the wind speed. The neutral drag coefficient is defined as $c_D = k^2/\ln^2(z_{\rm ref}/z_0)$, with κ the von Kármán constant and z_0 the surface roughness length. The net radiation is a prescribed function of time $Q_N(t) = -qt$ when $t < |Q_{N,\rm min}/q|$ and $Q_N(t) = Q_{N,\rm min}$ when $t \geq |Q_{N,\rm min}/q|$, with q a proportionality constant controlling the decay rate of Q_N. Both q and $Q_{N,\rm min}$ are considered known. The stability function is defined as $f(R_b) = (1 - \alpha R_b)^2$. Here, α is a fit parameter of the log-linear stability functions (Businger et al. 1971), and $R_b = (g/\theta_0)(z_{\rm ref}\Delta\theta)/U^2$ is the bulk Richardson number, with g the acceleration by gravity and θ_0 a reference temperature.

This model is a strong idealization of reality, especially since MOST may not be valid during the sunset transition (Sun et al. 2003). Nonetheless it is instructive to determine whether or not the model reproduces aspects of the observations. Equation (3) is numerically integrated for various combinations of $z_{\rm ref}$ and U.

The second model is an idealized SCM for the SBL (SBL-SCM). It solves the Reynolds-averaged equations for the two components of the horizontal wind vector profile (including the Coriolis force), the potential temperature profile, and the ground temperature as set up by Blackadar (1979). The model height is 5000 m and it uses a stretched grid with 100 vertical levels and the highest resolution near the surface. The turbulent diffusivities are modeled using the Prandtl mixing-length hypothesis and the standard Businger–Dyer relation to account for stable and slightly unstable conditions (Businger et al. 1971). The soil model is based on Blackadar (1976), and the radiation scheme is based on the effective atmospheric emissivity (Staley and Jurica 1972). Details may be found in A. M. Holdsworth and A. H. Monahan (2017, unpublished manuscript). Apart from an idealized treatment in the radiation scheme, the model neglects moisture effects.

RACMO is used with the aim to match the observations as closely as possible. The model was run daily for the period 2005–15 as a single-column model (RACMO-SCM) by Baas et al. (2017, manuscript submitted to *Bound.-Layer Meteor.*). The following model details are a summary of their work. RACMO-SCM is based on the ECMWF Integrated Forecast System (IFS), with specific parameterization details described in Baas et al. (2017, manuscript submitted to *Bound.-Layer Meteor.*). The main difference with the IFS model is that the first-order closure model was replaced with a prognostic turbulent kinetic energy (TKE) closure model, such that TKE is not forced to be in equilibrium (details in Lenderink and Holtslag 2004; Baas et al. 2017, manuscript submitted to *Bound.-Layer Meteor.*). The model has 90 vertical levels up to a height of 20 km. The grid spacing near the surface is approximately 6 m, with the lowest model level at 3 m. To investigate the effect of using a TKE scheme, the model was also run using the default IFS first-order closure for the years 2014–15. Further details on the computational details and the model physics may be found in ECMWF (2007). The model was initialized at 1200 UTC using the daily forecast output of the

three-dimensional RACMO, version 2.1 (van Meijgaard et al. 2008). The total model run spanned 48 h, but only the second 24-h period was used for the analysis.

3. Results

a. Inversion growth rate versus wind speed

Figure 2 shows the joint frequency distributions of $\Delta\theta_{\max}^{-1}\partial_t\Delta\theta$ (based on the potential temperature difference between 40 and 1.5 m), and its individual components $\Delta\theta_{\max}$ and $\partial_t\Delta\theta$, with the sunset wind speed U_{sunset} (also at 40 m) at Cabauw. Consistent with previous studies (e.g., Sun et al. 2012; van Hooijdonk et al. 2015; Monahan et al. 2015; van de Wiel et al. 2017) $\Delta\theta_{\max}$ suddenly increases when U_{sunset} is below 5–7 m s^{-1}. The red and blue curves indicate the joint frequency distributions using subsets of the observations based on the hidden Markov model. Broadly speaking, the VSBL (red) occurs when the wind is weak, while the WSBL (blue) occurs when the wind is strong. Note that these observations contain both cloudy- and clear-sky cases.

It is not surprising that the absolute growth rate $\partial_t\Delta\theta$ is closely related to $\Delta\theta_{\max}$ (Fig. 2b), since $\Delta\theta_{\max}$ is, in essence, the time integral of the growth rate. To investigate the qualitative differences, the inverse time scale is used. When this normalization was applied, no strong distinction between the regimes was evident (Fig. 2c). This fact is investigated further below.

To gain a more systematic insight into the wind dependence of the inverse time scale, Fig. 3a shows the median value of $\Delta\theta_{\max}^{-1}\partial_t\Delta\theta$ as a function of U_{sunset}, where for each case U_{sunset} was measured at z_2 (the highest level on which $\Delta\theta$ was based). The median is based on the subset of nights for which the sunset wind speed was in the interval $U_{\text{sunset}} \pm \delta$, with $\delta = 0.5$ m s^{-1} for Cabauw and Karlsruhe and $\delta = 1.0$ m s^{-1} for Dome C. Varying δ did not have a significant effect on the results, provided that sufficient nights were available per subset (not shown). Since at Dome C the observations spanned fewer years, and since only Antarctic summer nights could be used, a larger value of δ was chosen for this site. At the same time, the temporal structure at Dome C is generally smoother than at the other locations, and $\partial_t\Delta\theta$ could typically be determined with greater accuracy than at the other two sites. We also verified that using the mean value, instead of the median, did not have a significant effect on the results (not shown).

Figure 3a shows how $\Delta\theta_{\max}^{-1}\partial_t\Delta\theta$ depends on U_{sunset}. It shows an overall weak declining trend, with an apparent plateau at intermediate values of U_{sunset}. There is no indication that the development of nights that become very stable (red) is qualitatively different from nights that

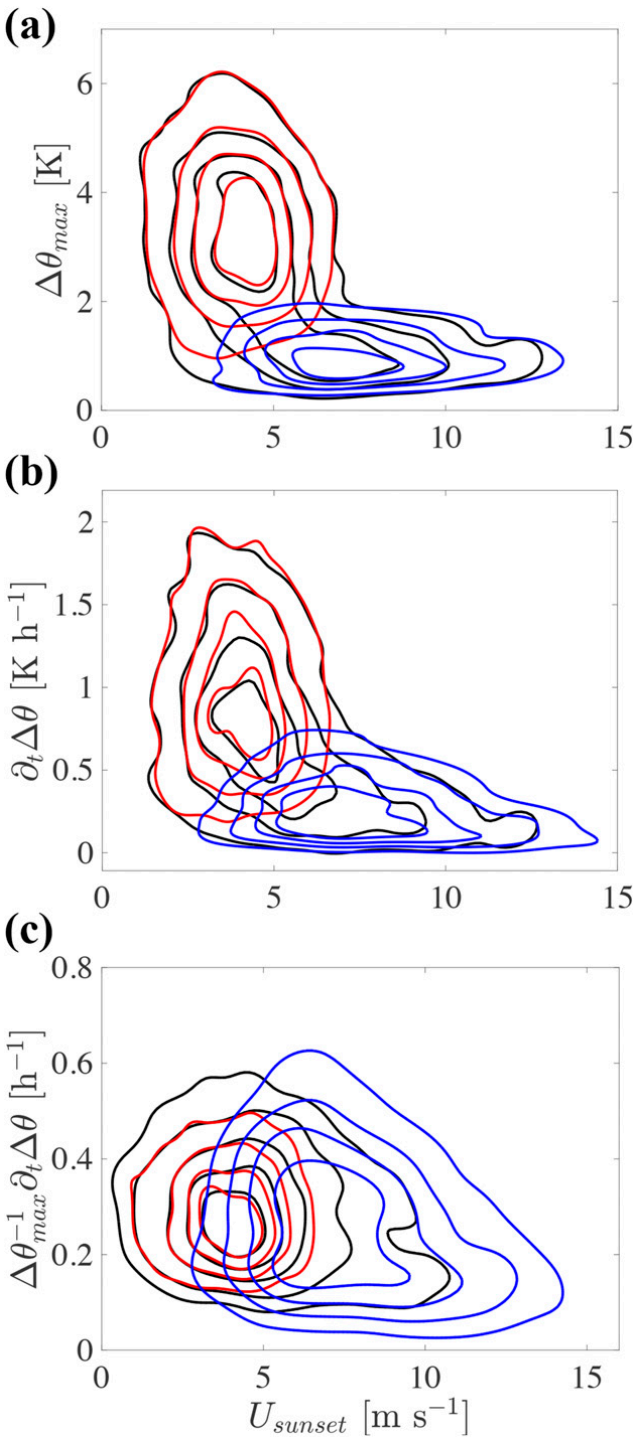

FIG. 2. Joint frequency distributions of the 40-m wind speed around sunset and (a) $\Delta\theta_{\max}(z = 40\text{–}1.5$ m), (b) $\partial_t\Delta\theta(z = 40\text{–}1.5$ m), and (c) $\Delta\theta_{\max}^{-1}\partial_t\Delta\theta(z = 40\text{–}1.5$ m) at Cabauw. The frequency distributions are estimated using an automated kernel density estimation (Botev et al. 2010). The isolines represent [0.2; 0.4; 0.6; 0.8] times the maximum of each distribution. The colors represent joint distributions of all nights in which the HMM state did not change within the first 5 h of the night (black), the subset in which the state corresponded to the VSBL (red), and the subset of nights in which the state corresponded to the WSBL (blue).

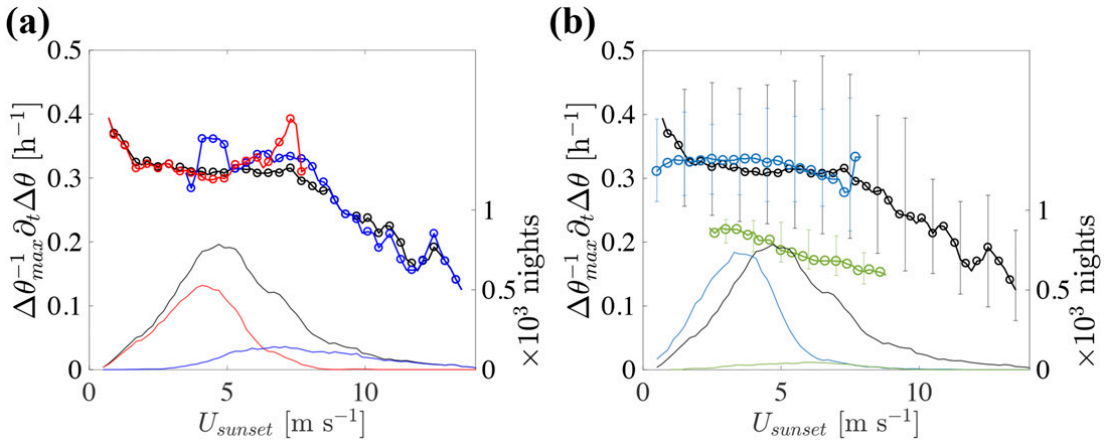

FIG. 3. (a) The median of $\Delta\theta_{\max}^{-1}\partial_t\Delta\theta$ as function of U_{sunset} at Cabauw. The median was calculated for each subset based on a range of U_{sunset}. The horizontal axis represents the center value of each subset. Colors represent all cases (black), all VSBL cases (red), and all WSBL cases (blue). (b) Comparison of the median inversion growth rate as function of U_{sunset} for three different sites: Cabauw (black), Karlsruhe (blue), and Dome C (green). The respective vertical ranges over which the temperature inversions were measured are 40–1.5, 60–2, and 18–0 m. The thin lines in both panels represent the number of nights ($\times 10^3$) available for each subset with the same color (right axes). The error bars illustrate the typical width of the distributions, which is measured by the 25th and 75th percentiles (i.e., 50% of the observations fall within the error bars).

become weakly stable (blue), even though the steady state may exhibit different dominant processes (van de Wiel et al. 2002; Mahrt 2014; van de Wiel et al. 2017). However, the region of overlap is limited to intermediate U_{sunset} only.

Figure 3b shows that the results from Karlsruhe and Dome C are remarkably consistent (i.e., in the range 0.2–0.4) with the observations at Cabauw, considering the differences among the sites. At Karlsruhe the range of U_{sunset} was limited, such that we could not investigate if a similar decrease occurred at higher U_{sunset}. The width of the distributions (the error bars) also complicate the interpretation of the observed trends. The observations at Dome C typically show lower values of $\Delta\theta_{\max}^{-1}\partial_t\Delta\theta$, which may be explained by the weaker diurnal cycle (Argentini et al. 2014); that is, the magnitude of the cycle of Q_N during a 24-h period is lower. This results in lower values of $\partial_t Q_N$ (Table 1), which is further investigated below. Nonetheless the trend appears to be weakly downward at this location as well. The error bars in Fig. 3 also show that Dome C exhibits much less variability. This results in narrower distributions, further demonstrating the suitability of this site for idealized, and conceptual, research.

Figure 4 indicates that the results in Fig. 3 are not sensitive to the measurement height of $\Delta\theta$ and U_{sunset}. A closer look suggests that the plateau as observed at Cabauw for Δz = 40–1.5 m is not a generic feature. For example, when the lower level is taken at z = 0.1 m, the decreasing trend appears more gradual. However, these differences fall well within the observed error bars. At Karlsruhe it is not clear if a trend over the relatively restricted range of U_{sunset} values is present at any measurement height. At Dome C the downward trend appears to be present, and it appears to be stronger below 20 m. A possible explanation is that the boundary layer is typically much shallower at this location than at the two midlatitude locations. As a result, the top of the tower may be outside of the boundary layer (Vignon et al. 2017).

b. *Width of the distributions*

The size of the error bars in Fig. 3b suggests that other parameters than U_{sunset} play an important role in determining $\Delta\theta_{\max}^{-1}\partial_t\Delta\theta$ as well. It also shows that the error bars at Dome C are smaller, which may be explained by the infrequent variations of moisture and cloud cover at this site (Lanconelli et al. 2011; Vignon et al. 2016). Moreover, measurements were used from a single season only.

The common factor of moisture, clouds, and season is that they are coupled (or at least correlated) to the evolution of Q_N and to each other. Therefore, it is difficult to investigate directly how each quantity is related to $\Delta\theta_{\max}^{-1}\partial_t\Delta\theta$. This is in contrast to U_{sunset}, which is a relatively independent parameter, in the sense that U_{sunset} is primarily a function the synoptic pressure gradient, while other parameters play a secondary role.

First, we investigate if high or low values of $\Delta\theta_{\max}^{-1}\partial_t\Delta\theta$ are systematically related to various Q_N-related quantities. For this purpose we use the percentile division as in Fig. 3b: the 25% slowest sunset transitions (based on $\Delta\theta_{\max}^{-1}\partial_t\Delta\theta$) of each subset are collected in a single group

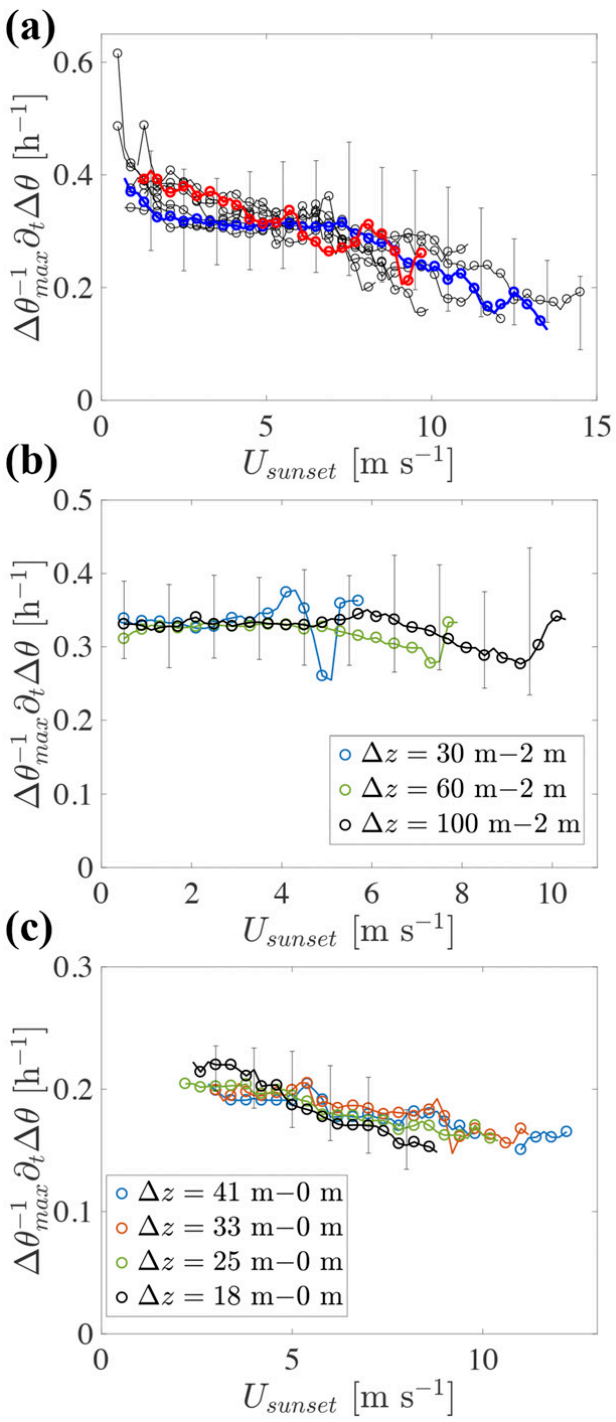

FIG. 4. (a) The median inversion growth rate as function of U_{sunset} at Cabauw for various measurement heights. The thin black lines indicate results for the levels 80–1.5, 20–1.5, 10–1.5, 80–0.1, 20–0.1, and 10–0.1 m. The colored lines represent levels that are discussed in the main text: 40–1.5 (blue) and 40–0.1 m (red). The other panels represent similar results for (b) Karlsruhe and (c) Dome C (see legend for the measurement heights). Error bars as in Fig. 3. Only the typical size of the error bars is shown for clarity.

(and similarly for each subsequent 25%). Figure 5a shows the ensemble-averaged time series of each group for the cloud cover, the relative humidity at 1.5 m, and the net radiation. This shows that, on average, nights with the lowest values of $\Delta\theta_{\text{max}}^{-1}\partial_t\Delta\theta$ are associated with higher levels of the cloud cover and the relative humidity. This may explain the lower (absolute) values of Q_N, both during the day and the night. However, Fig. 5b shows that winter (December–February) nights are disproportionally represented in the slowest 25%, which may also explain the weaker trend of Q_N.

A similar analysis was performed using several other quantities. We found no systematic relation with the wind direction, the absolute temperature, the friction velocity, the wind speed at 200 m, or the sensible heat flux (all before sunset). Therefore, we do not present results related to those quantities.

Next, we focus directly on how the evolution of the net radiation is related to $\Delta\theta_{\text{max}}^{-1}\partial_t\Delta\theta$. A similar approach is taken as for U_{sunset}, which essentially corresponds to treating $\partial_t Q_N$ (section 2) as an external parameter without explicit concern for the processes (such as clouds) that determined $\partial_t Q_N$ in a particular night. We define subsets based on nights with values for $\partial_t Q_N$ that are in the range $\partial_t Q_N \pm \delta$, where $\delta = 2.5\,\text{W m}^{-2}\,\text{h}^{-1}$ for Cabauw and $\delta = 0.5\,\text{W m}^{-2}\,\text{h}^{-1}$ for Dome C. Figure 6a shows the median $\Delta\theta_{\text{max}}^{-1}\partial_t\Delta\theta$ as a function of $\partial_t Q_N$. Consistent with Fig. 5, we observe a decrease when $\partial_t Q_N$ is small (in absolute sense) at Cabauw.

At Dome C the diurnal cycle of Q_N is weak, such that only a very narrow range of $\partial_t Q_N$ occurs. Consequently, no systematic comparison with Cabauw may be made. In fact, the close agreement is somewhat surprising. At Dome C the sky is often clear, and $\partial_t Q_N$ was determined with great accuracy. Conversely, at Cabauw low values of $|\partial_t Q_N|$ were typically observed during overcast conditions, which often resulted in poor estimates of $\partial_t Q_N$, owing to the irregular time series of Q_N. Although Fig. 6a is suggestive of a direct relationship of Q_N and its evolution with $\Delta\theta_{\text{max}}^{-1}\partial_t\Delta\theta$, the robustness of this relationship remains unclear.

Figure 6b shows essentially the same result based on $Q_{N,\text{min}}^{-1}\partial_t Q_N$, although it is less clear if a downward trend at low $Q_{N,\text{min}}^{-1}\partial_t Q_N$ is present owing to the size of the error bars. One may hypothesize that when the net radiation takes very long to reach its final state ($Q_{N,\text{min}}^{-1}\partial_t Q_N \to 0$), also the evolution of the temperature inversion should be very slow ($\Delta\theta_{\text{max}}^{-1}\partial_t\Delta\theta \to 0$). Following this reasoning, possible support for a trend in Fig. 6b is that for low values of $Q_{N,\text{min}}^{-1}\partial_t Q_N$, the system evolves so slowly that it is close to local equilibrium and $\Delta\theta_{\text{max}}^{-1}\partial_t\Delta\theta$ is directly related to $Q_{N,\text{min}}^{-1}\partial_t Q_N$. Conversely, when $Q_{N,\text{min}}^{-1}\partial_t Q_N \to \infty$ (i.e., the sunset

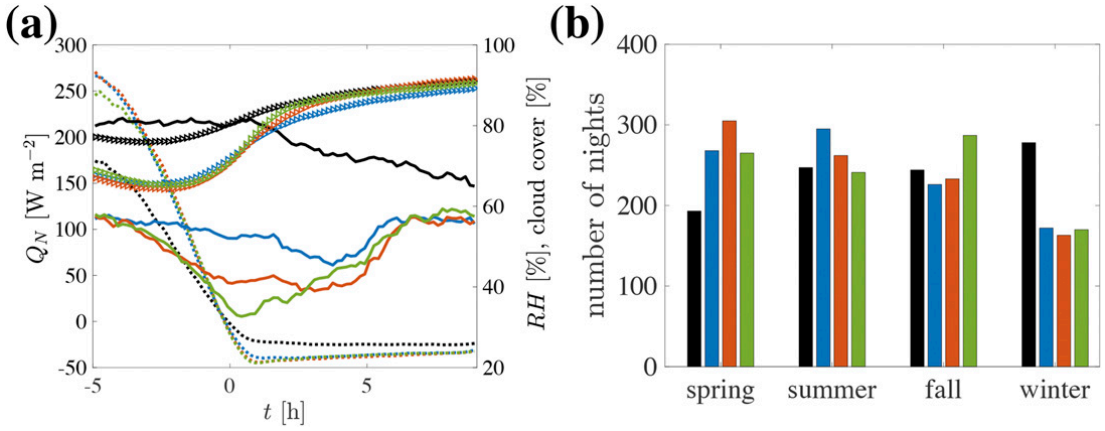

FIG. 5. (a) Ensemble-averaged time series of Q_N (dotted; left axis), the cloud cover (solid; right axis), and the relative humidity (triangles; right axis) at Cabauw. The black line represents the collection of nights from all classes of U_{sunset} with an inverse time scale between the 0th and 25th percentiles. Other colors represent the same for the 25th–50th (blue), 50th–75th (red), and 75th–100th percentile ranges (green). (b) Number of the nights that were suitable for analysis (i.e., $\eta^2 < 0.02$) per season for each quartile. Colors are as in (a).

transition occurs instantaneously), the system is not in local equilibrium with the evolution of Q_N; hence, $Q_{N,\text{min}}^{-1}\partial_t Q_N$ is no longer a relevant time scale for $\Delta\theta_{\text{max}}^{-1}\partial_t\Delta\theta$, and the curve levels off.

c. Numerical models

The observations suggest that $\Delta\theta_{\text{max}}^{-1}\partial_t\Delta\theta$ takes a relatively small range of values (0.2–0.4 h^{-1}) and it decreases slightly with increasing U_{sunset}. It is not clear what physical processes control this relation, as U_{sunset} is not an externally imposed control parameter, but it is a boundary layer quantity dynamically coupled to the various other quantities we are considering. Therefore, we use three types of numerical models, such that a more controlled test may be performed. Information on which type(s) of model(s) reproduce(s) the trend of the observations could give an indication of what dynamics are responsible.

Given the idealized nature of the bulk model, its use for studying the effect of the wind speed provides qualitative insight only. Nonetheless, it would be highly advantageous if such a model is sufficient to explain the observations, since it provides the most direct mechanistic insight. As a first step, one could approach the SBL growth as a simple diffusion problem, which is governed by a time scale z_{ref}^2/K, with $K = \kappa u_* z_{\text{ref}}$ the turbulent diffusivity (chosen equal for heat and momentum). The effect of the wind speed is twofold. First, a larger wind speed would increase the turbulent diffusivity and, therefore, reduce the time scale. Conversely, increasing U_{sunset} would also increase the characteristic length scale, such as the Obukhov length, the boundary layer height

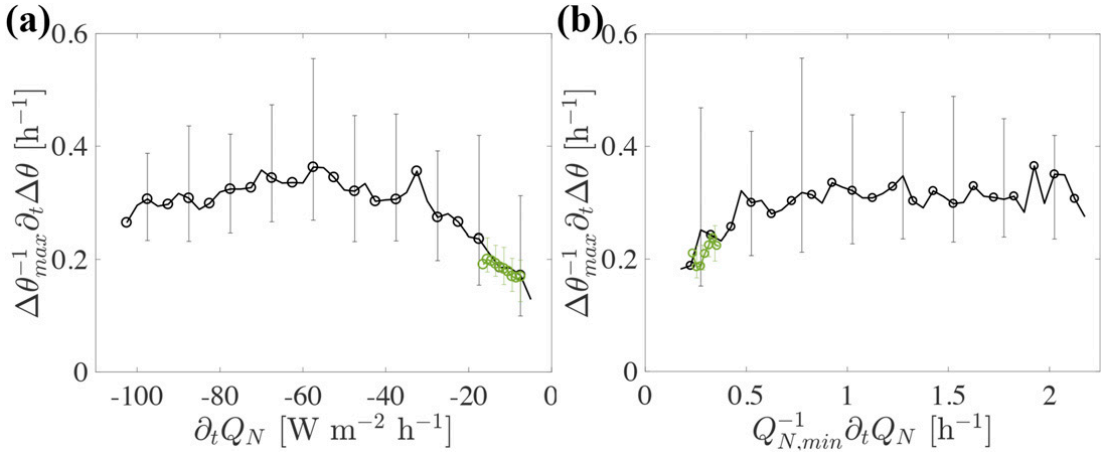

FIG. 6. (a) The median inversion growth rate as function of $\partial_t Q_N$ for Cabauw (black) and Dome C (green). Error bars are as in Fig. 3. (b) As in (a), but normalized using $Q_{N,\text{min}}$.

(André and Mahrt 1982), or the crossing level (van de Wiel et al. 2012). To account for this effect, z_{ref} in Eq. (3) should increase, which increases the turbulent time scale. The bulk model is used to investigate both effects.

Figure 7a shows that, at a fixed z_{ref}, the evolution of the normalized inversion strength in all cases follows more or less the same slope, which is dictated by the magnitude of Q_N/c_v [Eq. (3)]. This indicates that the turbulent heat flux and the net radiation are always close to balance, which is due to the simplicity of the model. The small differences in slope between the curves are caused by variations in U_{40}, which represents U_{sunset} at 40 m. When U_{sunset} was increased, while keeping z_{ref} constant, the initial growth of $\Delta\theta_{max}^{-1}\partial_t\Delta\theta$ was indeed larger. To test the effect of z_{ref}, U_{sunset} should not be kept constant, since then increasing z_{ref} would effectively decrease the turbulent mixing. Therefore, we vary z_{ref} while modifying U_{sunset} such that the neutral friction velocity $u_{*N} = c_D^{1/2}U_{sunset}$ is kept constant. Figure 7b shows opposite results from Fig. 7a; that is, the growth rate of $\Delta\theta_{max}^{-1}\Delta\theta$ was reduced at higher z_{ref} and U. In summary, since both effects work in opposite direction, the bulk model remains inconclusive on the compound effect on the evolution of $\Delta\theta_{max}^{-1}\Delta\theta$.

In the SBL-SCM both the wind speed and a vertical length scale are dynamic quantities that result from the imposed geostrophic wind speed, the surface properties, and the initial conditions. If the results would be consistent with the observations, this would imply that the compound effect of U_{sunset} on the turbulent mixing and the vertical length scale is sufficient to explain the observed trend in Fig. 3. However, Fig. 8a shows that an increased geostrophic wind (and thus U_{sunset}) accelerates the growth of $\Delta\theta_{max}^{-1}\Delta\theta$. Since the rudimentary soil model is not tuned to any of the observational sites, we investigate the sensitivity of the evolution of $\Delta\theta/\Delta\theta_{max}$ to the soil model. Figure 8a shows that the results are comparable between dry clay and fresh snow. In fact, a wide variety of other soil types gave very similar results initially in the sense that the normalized inversion grew faster with increasing wind speed (not shown). As such, we cannot attribute the poor representation of the sunset transition in this model to the particular choice of soil type.

The qualitative disagreement with the observations may be explained partially by the invalidity of the equilibrium flux-gradient relations during the sunset transition. Moreover, the model is initialized right before the onset of the SBL, such that the SBL growth is very sensitive to the initial conditions (Fig. 8b). In fact, model simulations are more sensitive to the initial conditions than to the soil type. Thus, although the model provides useful insight in the relation between the model parameters and dynamics after the sunset transition, it appears less suitable to model the transition itself.

Since the idealized models do not provide qualitative similarities with the observations, we also investigate a more realistic model. The RACMO-SCM with a TKE scheme (as in Baas et al. 2017, manuscript submitted to *Bound.-Layer Meteor.*) does not rely on a first-order parameterization of turbulence. Additionally, this model is more elaborate than the SBL-SCM, in the sense that it models a full diurnal cycle with a simplified representation of horizontal advection and moisture schemes and more advanced radiation and soil schemes. Therefore, we may expect that the model provides a more realistic representation of the SBL transition.

Figure 9a shows the median of $\Delta\theta_{max}^{-1}\partial_t\Delta\theta$ (similar to Fig. 4). It shows that reasonable agreement with the observations was obtained, especially at higher wind speeds. Modeled time series are typically smoother than observational time series. Therefore, a slightly smaller value of $\Delta\theta_{max}$ in the model is not surprising and the overestimation of the inversion growth rate by the model could be due to this fact. However, the variation among various model levels is in contrast with observations (cf. Fig. 4) and suggests that the model is still prone to other biases. Moreover, the increase at very low wind speeds should be approached with caution, since these types of models typically do not perform well in this range. Figure 9b shows that there also is a systematic overestimation by the model, when the sensitivity to the evolution of the net radiation was investigated. The shapes of the curves are nonetheless qualitatively similar.

The reasonable agreement between the RACMO-SCM and the observations could be explained by the more realistic prognostic representation of the TKE in this model. To test this hypothesis, a new set of runs was performed (spanning 2 years of observations) using the first-order IFS closure for turbulence of the ECMWF. Figure 9a shows that this severely reduces the model performance. The reduction of the performance is almost completely due to the poor prediction of $\partial_t\Delta\theta$, while reasonable agreement between the two schemes was found for $\Delta\theta_{max}$ (not shown). Nonetheless, it is clear that between the SBL-SCM and the RACMO-SCM with the IFS scheme a substantial qualitative improvement was already achieved. The use of a prognostic TKE scheme provided another significant improvement step (Fig. 9a).

In summary, the bulk model and the SBL-SCM appeared to be unable to provide qualitative agreement with the observations. This suggests that the physical processes of particular importance are either absent or poorly represented in these models. A first qualitative important improvement is observed when the RACMO-SCM with the IFS scheme is used, which we attribute to the fact that a

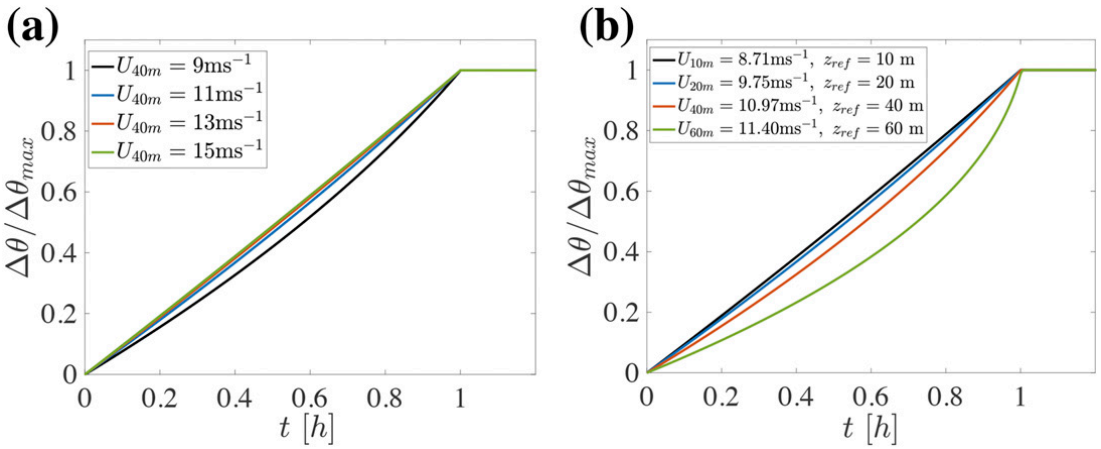

FIG. 7. (a) Temporal evolution of the normalized temperature inversion for various values of U (see legend) and $z_{\text{ref}} = 40$ m in the bulk model. (b) As in (a), but for varying combinations of U and z_{ref} (see legend) such that $u_* = 0.6\,\text{m s}^{-1}$.

full diurnal cycle was modeled, and thus that a realistic and coherent state of the boundary layer was known at the time of the onset of the SBL. Further improvement by using the TKE scheme suggests that the history of the boundary layer is important in a more general sense. This seems to be consistent with the notion that turbulence is not in local equilibrium (e.g., Blay-Carreras et al. 2014).

4. Discussion

In this paper, we investigated the relation between the growth of the SBL across the evening transition and other physical quantities. For this approach it was necessary to use a statistical fitting procedure, which neglects the large variety in how the temperature inversion may develop in individual cases.

Previous studies found strong relations between the wind shear and the temperature inversion (Sun et al. 2012; van Hooijdonk et al. 2015), which could be explained using a strongly idealized model (van de Wiel et al. 2012, 2017). Furthermore, evidence was found of at least two distinct regimes in the SBL (Grachev et al. 2005; Banta et al. 2007; van Hooijdonk et al. 2015; Monahan et al. 2015), of which the most stable regime seems incompatible with MOST-type scaling laws (Sorbjan 2010; Mahrt 2014). Considering the distinct behavior between the regimes later in the night, it would not have been surprising if signals of distinct development were detected at an earlier stage. However, once normalized by the maximum temperature inversion, it appears there is little evidence of distinct regimes (Fig. 3). A possible explanation is that the

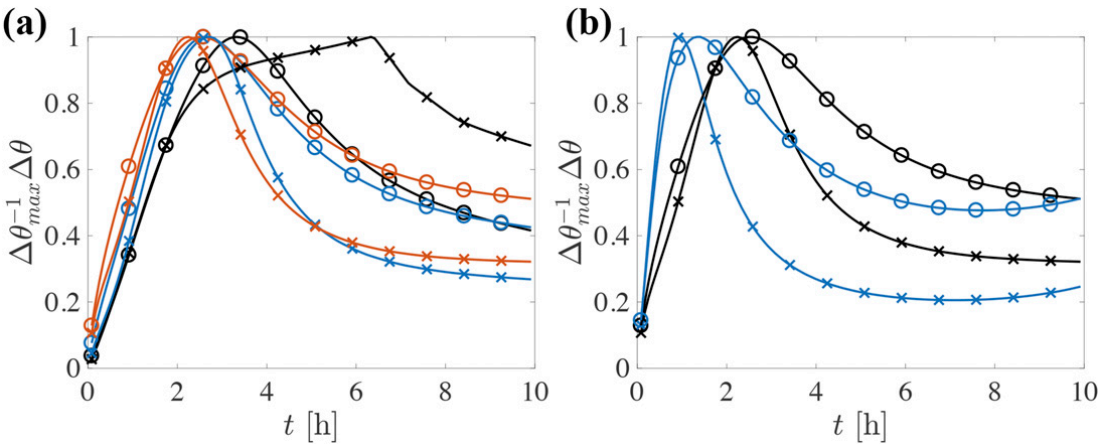

FIG. 8. (a) Time series of the normalized temperature inversion for dry clay (circles), and fresh snow (crosses) for various values of geostrophic wind: 10 (black), 14 (blue), and 18 m s^{-1} (red) in the SBL-SCM. Note that for 10 m s^{-1}, the fresh snow case shows signs of a collapse of turbulence. (b) Time series of the normalized temperature inversion for a geostrophic wind of 18 m s^{-1} for the same initial conditions as in (a) (black), and using the profile at $t = 3$ h (blue). Symbols are as in (a).

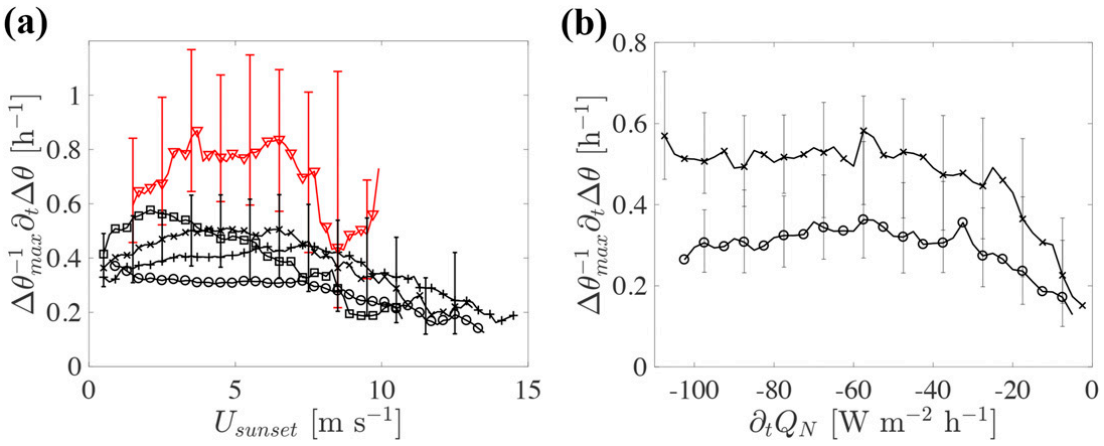

FIG. 9. (a) The median inversion growth rate as function of U_{sunset} at Cabauw, similar to Fig. 3. The circles represent the observed values (Δz = 40–1.5 m). The squares, crosses, and plus signs indicate the RACMO-SCM results using the TKE scheme at various measurement levels, that is, 20–2, 40–2, and 80–2 m, respectively. The red downward triangles are the results of the RACMO-SCM using the IFS scheme. The error bars are also as in Fig. 3. (b) The median inversion growth rate as function of $\partial_t Q_N$, similar to Fig. 6. Circles and crosses are as in (a).

initial growth is dominated by the same processes (e.g., continuous turbulence or remnants of convective motions). At a later stage turbulence may be weak and intermittent, such that other processes (e.g., the ground heat flux) may be more significant (van de Wiel et al. 2017). In fact, the wind shear appeared to have only a very mild effect on $\Delta\theta_{\text{max}}^{-1}\partial_t\Delta\theta$. We hypothesize that the weak effect of the wind may be due to counteracting processes: a stronger wind shear leads to more mixing but also to a deeper boundary layer (i.e., more available warm air). Other possibilities may be a relation to the weaker decay of convective turbulence in case wind shear is strong (Pino et al. 2006).

Pattantyús-Ábrahám and Jánosi (2004) suggested that the tropospheric water content was the most important factor in the evolution of the nocturnal temperature. Our observations indicate that very low (absolute) values of $\partial_t Q_N$ (associated with clouds, moisture, and season) may lead to slower growth of $\Delta\theta_{\text{max}}^{-1}\partial_t\Delta\theta$. Additionally, the results showed that moisture-related dynamics (e.g., clouds) may partly account for the spread in $\Delta\theta_{\text{max}}^{-1}\partial_t\Delta\theta$. It is unfortunate that Pattantyús-Ábrahám and Jánosi (2004) did not investigate the time scale in relation to Q_N, since Q_N (and its evolution), moisture and clouds, and the seasonal cycle are coupled and/or correlated. As a result, disentangling effects of individual parameters is complicated.

To further complicate the problem, we found indications that the daytime evolution (e.g., how the CBL decays) may be an important factor that affects the SBL growth (Fig. 9). This would explain why no, or only weak, relations were found with many contemporaneously measured variables (e.g., wind speed, temperature, humidity). Since these quantities contain little information on the SBL growth, it seems unlikely that a simple physical model assuming instantaneous equilibrium of turbulent fluxes to the resolved state could qualitatively reproduce the early SBL growth, and how this growth depends on the various parameters.

Consistent with the present results, Edwards (2009) observed clear temporal differences depending on whether or not the full diurnal cycle was modeled. A plausible explanation is that when a full diurnal cycle is being modeled, the flow constitutes a physically realizable state at the time of the onset of the SBL. The archetypal neutral boundary layer (a logarithmic wind profile and no temperature gradients) may not be a realistic state of the boundary layer at any time around sunset. Consequently, they cannot reproduce important aspects of the transient SBL (Figs. 7 and 8). This suggests that at least the presunset history (i.e., the afternoon decay of convective turbulence) should be taken into account in models that aim to study the onset of the SBL.

The results of Jensen et al. (2016) also suggest that the presunset state is important for the dynamics at sunset. They investigated detailed flow characteristics during this presunset period, and they found that the (third order) budget terms of the sensible heat flux contain clues about the nature of the countergradient fluxes around sunset. However, it remains unclear if these budget terms qualitatively impact the growth rate of the temperature inversion, since the RACMO-SCM is able to reproduce the inversion growth with reasonable accuracy, even though it does not resolve third-order terms.

The studies of De Wekker and Whiteman (2006) and Pattantyús-Ábrahám and Jánosi (2004) shared similar approaches to determine a typical evolution of the SBL. These approaches were distinct from this study, but they

are related in the sense that, in first-order approximation, a fixed functional form was used to fit the temporal evolution of a temperature-based quantity. For a set of 18 individual nights from 9 different locations, De Wekker and Whiteman (2006) used an exponential function to the normalized cumulative cooling during the whole night. The time scale that they found ranged from 3 to 7.5 h, corresponding to a rate of ~0.13–0.33 h^{-1}. The related approach by Pattantyús-Ábrahám and Jánosi (2004) yielded values for the inverse time scale of 0.1–0.5 h^{-1}, compared to the scale of 0.2–0.4 h^{-1} that we found at three distinct sites. As such, there appears to be some generality to the evolution rate of the SBL among studies, locations, measurement heights (Fig. 4), and a broad range of conditions. So despite the complexity of the dynamics, a simple ad hoc model for the evolution of the SBL (or at least the temperature inversion) may be sufficient to be useful in studies that do not require detailed insight in the boundary layer itself. The consistency among sites could be further verified by performing a similar analysis on a large number of sites [e.g., as in Monahan et al. (2011)]. Of course, such an analysis could not achieve the same level of detail per site, but it could reveal a systematic dependence on other parameters, such as soil characteristics.

Since at Dome C clouds are mostly absent and conditions are dry in general, the diurnal cycle of Q_N is mostly determined by the zenith angle. Therefore, an alternative approach would be to conduct a more detailed investigation of this site. This might not only be beneficial for understanding the evolution of the SBL, but also for the decay of the CBL. With respect to the latter, Sorbjan (1997) used large-eddy simulation to find that turbulence decreases faster when Q_N decreases more abruptly (i.e., smaller $\partial_t Q_N$; note that $\partial_t Q_N$ is negative), which is consistent with the bulk model and may explain the slower dynamics when $\partial_t Q_N$ is less negative (i.e., at Dome C, or when there are clouds).

Finally, we found that an operation-level SCM results in reasonable agreement in terms of statistics. Unfortunately these models are typically complex and may behave unexpectedly if dynamical features (such as clouds) are turned off, which makes them less versatile than more idealized models. It may be possible, however, to investigate the effect of small perturbations of preexisting cases to gain insight in the effect on the growth of the temperature inversion.

5. Conclusions

A large number of observations from three distinct sites were used to study the growth of the SBL, as measured by the temperature inversion. The results show remarkable consistency of the normalized growth rate among these sites. The sensitivity to several parameters was tested and, similar to Pattantyús-Ábrahám and Jánosi (2004), most of these parameters did not indicate a systematic relation with the growth rate. Previous studies identified the wind speed as a key parameter for the structure of the established SBL (e.g., Sun et al. 2012; van de Wiel et al. 2012). Consistent with these studies, we observe that the absolute growth of the temperature inversion sharply increases once the wind is below a critical range. Once normalized by the ultimate inversion strength, the inverse time scale does not show clear evidence of multiple regimes. This suggests that the early development of the SBL is dominated by the same dynamical processes, and the qualitatively distinct regimes become apparent later. Moreover, the present results suggest at most a very weakly decreasing dependence of the normalized growth rate with increasing wind speed.

A clearer trend was found when the decay of the net radiation $\partial_t Q_N$ (or $Q_{N,\min}\partial_t Q_N$) was close to zero. In that case, $\Delta\theta_{\max}^{-1}\partial_t\Delta\theta$ appeared to attain lower values. However, $\partial_t Q_N$ could not be related to a single physical mechanism. Moreover, no relation was found once $\partial_t Q_N$ became more negative.

To further investigate the underlying mechanisms, numerical models were used. These showed that a simple bulk model, or the SBL-SCM, could not replicate the dependency on the wind speed, despite the qualitative success of similar models in describing the (quasi) steady state of the SBL (A. M. Holdsworth and A. H. Monahan 2017, unpublished manuscript; van de Wiel et al. 2017). The RACMO-SCM is capable of modeling the full diurnal cycle and it provided similar statistics to the observations when the TKE scheme was used, while the first-order IFS scheme resulted in qualitative similarities only. This suggests the importance of the history of the system in terms of TKE and the mean flow properties of the whole boundary layer for the sunset transition and the early SBL growth.

Acknowledgments. The authors thank Christoph Genthon for providing the Dome C meteorological data, the French polar institute (IPEV, CALVA program 1013) for the logistical support, and the WRMC-BSRN network, Angelo Lupi, and Christian Lanconelli for dissemination of the Dome C radiation data. We also thank Martin Kohler and the Institute for Meteorology and Climate Research of Karlsruhe Institute of Technology (KIT) for providing the Karlsruhe observations. Fred Bosveld and the Royal Dutch Meteorological Institute (KMNI) are thanked for the freely available

Cabauw observations. The following funding agencies are acknowledged for their contribution: IvH is supported by the Netherlands Organisation for Scientific Research (NWO, ALW Grant 832010110); AHM, AH, and CA are supported by the Natural Sciences and Engineering Research Council Canada; and BvdW and PB are supported by an ERC Consolidator grant (648666). Finally, the University of Victoria is thanked for hosting IvH during several weeks for this research.

APPENDIX

Fitting Procedure

The fitting procedure was aimed at estimating a "typical" inversion growth rate for each night, measured by $\partial_t \Delta\theta$. Considering the irregularity of the time series, different choices of fitting procedure may lead to a better fit for some nights and a poorer fit for others. The procedure described below appeared to be reasonably robust, in the sense that the quality of the fit resembled the irregularity within a particular night.

The procedure used $\Delta\theta$ (measured over a certain vertical range) and the net radiation. Furthermore the time is defined relative to sunset; that is, we defined $t = 0$ when $Q_N = 0$. There are several main steps in the procedure:

First, the time was located when the stable boundary layer (SBL) starts—that is, when $\Delta\theta$ crosses zero just before sunset. This time is defined as $t_{\min}$. Next, the maximum inversion $\Delta\theta_{\max}$ was determined, and $t_{\max}$ was defined as the time when $\Delta\theta = 0.9\Delta\theta_{\max}$ for the first time after sunset. We found that using 90% of the maximum leads to less sensitivity to spikes.

Third, the minimum value of $\Delta\theta$ was subtracted from the time series, since Eq. (1) starts at 0, while $\Delta\theta$ is slightly negative during the day.

The *lsqcurvefit* function of MATLAB was used to fit Eq. (1) to the shifted $\Delta\theta$–time series of each day between $t = t_{\min} + a$ and $t = t_{\max} + b$, where $a = [0, -2, -1, -2, -1, -1, 0]$ and $b = [0, 0, 0.5, 1, 0, 1, 1]$. This means that seven distinct fits were made for each day. No fits were made when fewer than five observations were available. Figure 1 in section 2c shows two examples of a fit for two different nights. For each fit the typical evolution $\partial_t \Delta\theta = kT/4$ was determined.

Finally, for each night, the extremes were removed, i.e., the two highest and two lowest estimates of $\partial_t \Delta\theta$ were omitted. The remaining three estimates were then averaged to give a final estimate of $\partial_t \Delta\theta$, which was used for the analysis.

To determine $\partial_t Q_N$ a similar procedure was used. First, we define $Q_{N,\max}$ the maximum of Q_N in the time interval $-4 < t < 0$ h and $Q_{N,\min}$ the minimum in the interval $0 < t < 5$ h. Again we define $t_{\min}$ and $t_{\max}$. The time when Q_N becomes less than $0.9Q_{N,\max}$ was used as $t_{\min}$ and the time when Q_N becomes less (more negative) than $0.9Q_{N,\min}$ was used as $t_{\max}$. A linear function $f(t) = a_1 t + a_0$ was used to fit the time series between $t = t_{\min} + a$ and $t = t_{\max} + b$. The mean value of the middle three values of a_1 was then used as an estimate of $\partial_t Q_N$.

REFERENCES

Acevedo, O. C., L. Mahrt, F. S. Puhales, F. D. Costa, L. E. Medeiros, and G. A. Degrazia, 2016: Contrasting structures between the decoupled and coupled states of the stable boundary layer. *Quart. J. Roy. Meteor. Soc.*, **142**, 693–702, doi:10.1002/qj.2693.

André, J. C., and L. Mahrt, 1982: The nocturnal surface inversion and influence of clear-air radiative cooling. *J. Atmos. Sci.*, **39**, 864–878, doi:10.1175/1520-0469(1982)039<0864:TNSIAI>2.0.CO;2.

Ansorge, C., and J. P. Mellado, 2016: Analyses of external and global intermittency in the logarithmic layer of Ekman flow. *J. Fluid Mech.*, **805**, 611–635, doi:10.1017/jfm.2016.534.

Argentini, S., I. Pietroni, G. Mastrantonio, A. P. Viola, G. Dargaud, and I. Petenko, 2014: Observations of near surface wind speed, temperature and radiative budget at Dome C, Antarctic Plateau during 2005. *Antarct. Sci.*, **26**, 104–112, doi:10.1017/S0954102013000382.

Armenio, V., and S. Sarkar, 2002: An investigation of stably stratified turbulent channel flow using large-eddy simulation. *J. Fluid Mech.*, **459**, 1–42, doi:10.1017/S0022112002007851.

Banta, R. M., L. Mahrt, D. Vickers, J. Sun, B. B. Balsley, Y. L. Pichugina, and E. J. Williams, 2007: The very stable boundary layer on nights with weak low-level jets. *J. Atmos. Sci.*, **64**, 3068–3090, doi:10.1175/JAS4002.1.

Basu, S., J.-F. Vinuesa, and A. Swift, 2008: Dynamic LES modeling of a diurnal cycle. *J. Appl. Meteor. Climatol.*, **47**, 1156–1174, doi:10.1175/2007JAMC1677.1.

Blackadar, A. K., 1976: Modeling nocturnal boundary layer. *Bull. Amer. Meteor. Soc.*, **57**, 631–631.

——, 1979: High resolution models of the planetary boundary layer. *Adv. Environ. Sci. Eng.*, **1**, 50–85.

Blay-Carreras, E., E. R. Pardyjak, D. Pino, D. Alexander, F. Lohou, and M. Lothon, 2014: Countergradient heat flux observations during the evening transition period. *Atmos. Chem. Phys.*, **14**, 9077–9085, doi:10.5194/acp-14-9077-2014.

Botev, Z. I., J. F. Grotowski, and D. P. Kroese, 2010: Kernel density estimation via diffusion. *Ann. Stat.*, **38**, 2916–2957, doi:10.1214/10-AOS799.

Businger, J. A., J. C. Wyngaard, Y. Izumi, and E. F. Bradleu, 1971: Flux-profile relationships in the atmospheric boundary layer. *J. Atmos. Sci.*, **28**, 181–189, doi:10.1175/1520-0469(1971)028<0181:FPRITA>2.0.CO;2.

De Wekker, S. F. J., and C. D. Whiteman, 2006: On the time scale of nocturnal boundary layer cooling in valleys and basins and over plains. *J. Appl. Meteor. Climatol.*, **45**, 813–820, doi:10.1175/JAM2378.1.

ECMWF, 2007: IFS documentation—Cy31r1. Part IV: Physical processes. ECMWF Tech. Rep., 155 pp., https://www.ecmwf.int/sites/default/files/elibrary/2007/9221-part-iv-physical-processes.pdf.

Edwards, J. M., 2009: Radiative processes in the stable boundary layer: Part II. The development of the nocturnal

boundary layer. *Bound.-Layer Meteor.*, **131**, 127–146, doi:10.1007/s10546-009-9363-9.

——, 2011: Radiation and turbulence in the stable boundary layer. *Proc. GABLS Workshop on Diurnal Cycles and the Stable Boundary Layer*, Reading, United Kingdom, ECMWF, 7–10, https://www.ecmwf.int/sites/default/files/elibrary/2012/9261-radiation-and-turbulence-stable-boundary-layer.pdf.

Genthon, C., D. Six, H. Gallée, P. Grigioni, and A. Pellegrini, 2013: Two years of atmospheric boundary layer observations on a 45-m tower at Dome C on the Antarctic plateau. *J. Geophys. Res. Atmos.*, **118**, 3218–3232, doi:10.1002/jgrd.50128.

Grachev, A. A., C. Fairall, P. O. G. Persson, E. L Andreas, and P. S. Guest, 2005: Stable boundary-layer scaling regimes: The SHEBA data. *Bound.-Layer Meteor.*, **116**, 201–235, doi:10.1007/s10546-004-2729-0.

——, E. L Andreas, C. W. Fairall, P. S. Guest, and P. O. G. Persson, 2013: The critical Richardson number and limits of applicability of local similarity theory in the stable boundary layer. *Bound.-Layer Meteor.*, **147**, 51–82, doi:10.1007/s10546-012-9771-0.

Holtslag, A. A. M., and Coauthors, 2013: Stable atmospheric boundary layers and diurnal cycles: Challenges for weather and climate models. *Bull. Amer. Meteor. Soc.*, **94**, 1691–1706, doi:10.1175/BAMS-D-11-00187.1.

Jensen, D. D., D. F. Nadeau, S. W. Hoch, and E. R. Pardyjak, 2016: Observations of near-surface heat-flux and temperature profiles through the early evening transition over contrasting surfaces. *Bound.-Layer Meteor.*, **159**, 567–587, doi:10.1007/s10546-015-0067-z.

Kalthoff, N., and B. Vogel, 1992: Counter-current and channelling effect under stable stratification in the area of Karlsruhe. *Theor. Appl. Climatol.*, **45**, 113–126, doi:10.1007/BF00866400.

Lanconelli, C., M. Busetto, E. G. Dutton, G. König-Langlo, M. Maturilli, R. Sieger, V. Vitale, and T. Yamanouchi, 2011: Polar baseline surface radiation measurements during the International Polar Year 2007–2009. *Earth Syst. Sci. Data*, **3**, 1–8, doi:10.5194/essd-3-1-2011.

Lenderink, G., and A. A. M. Holtslag, 2004: An updated length-scale formulation for turbulent mixing in clear and cloudy boundary layers. *Quart. J. Roy. Meteor. Soc.*, **130**, 3405–3427, doi:10.1256/qj.03.117.

Lothon, M., and Coauthors, 2014: The BLLAST field experiment: Boundary-layer late afternoon and sunset turbulence. *Atmos. Chem. Phys.*, **14**, 10 931–10 960, doi:10.5194/acp-14-10931-2014.

Mahrt, L., 2014: Stably stratified atmospheric boundary layers. *Annu. Rev. Fluid Mech.*, **46**, 23–45, doi:10.1146/annurev-fluid-010313-141354.

Monahan, A. H., Y. He, N. McFarlane, and A. Dai, 2011: The probability distribution of land surface wind speeds. *J. Climate*, **24**, 3892–3909, doi:10.1175/2011JCLI4106.1.

——, T. Rees, Y. He, and N. McFarlane, 2015: Multiple regimes of wind, stratification, and turbulence in the stable boundary layer. *J. Atmos. Sci.*, **72**, 3178–3198, doi:10.1175/JAS-D-14-0311.1.

Monin, A. S., 1970: The atmospheric boundary layer. *Annu. Rev. Fluid Mech.*, **2**, 225–250, doi:10.1146/annurev.fl.02.010170.001301.

Nadeau, D. F., E. R. Pardyjak, C. W. Higgins, H. J. S. Fernando, and M. B. Parlange, 2011: A simple model for the afternoon and early evening decay of convective turbulence over different land surfaces. *Bound.-Layer Meteor.*, **141**, 301–324, doi:10.1007/s10546-011-9645-x.

Nieuwstadt, F. T. M., and H. Tennekes, 1981: A rate equation for the nocturnal boundary-layer height. *J. Atmos. Sci.*, **38**, 1418–1428, doi:10.1175/1520-0469(1981)038<1418:AREFTN>2.0.CO;2.

Pattantyús-Ábrahám, M., and I. M. Jánosi, 2004: What determines the nocturnal cooling timescale at 2 m? *Geophys. Res. Lett.*, **31**, L05109, doi:10.1029/2003GL019137.

Pino, D., H. J. J. Jonker, J. V.-G. de Arellano, and A. Dosio, 2006: Role of shear and the inversion strength during sunset turbulence over land: Characteristic length scales. *Bound.-Layer Meteor.*, **121**, 537–556, doi:10.1007/s10546-006-9080-6.

Sorbjan, Z., 1997: Decay of convective turbulence revisited. *Bound.-Layer Meteor.*, **82**, 503–517, doi:10.1023/A:1000231524314.

——, 2006: Local structure of turbulence in stably stratified boundary layers. *J. Atmos. Sci.*, **63**, 1526–1537, doi:10.1175/JAS3704.1.

——, 2010: Gradient-based scales and similarity laws in the stable boundary layer. *Quart. J. Roy. Meteor. Soc.*, **136**, 1243–1254, doi:10.1002/qj.638.

Staley, D. O., and G. M. Jurica, 1972: Effective atmospheric emissivity under clear skies. *J. Appl. Meteor.*, **11**, 349–356, doi:10.1175/1520-0450(1972)011<0349:EAEUCS>2.0.CO;2.

Stull, R. B., 1983: Integral scales for the nocturnal boundary layer. Part 1: Empirical depth relationships. *J. Climate Appl. Meteor.*, **22**, 673–686, doi:10.1175/1520-0450(1983)022<0673:ISFTNB>2.0.CO;2.

——, 2000: *Meteorology for Scientists and Engineers.* 2nd ed. Brooks Cole, 528 pp.

Sun, J., S. P. Burns, A. C. Delany, S. P. Oncley, T. W. Horst, and D. H. Lenschow, 2003: Heat balance in the nocturnal boundary layer during CASES-99. *J. Appl. Meteor.*, **42**, 1649–1666, doi:10.1175/1520-0450(2003)042<1649:HBITNB>2.0.CO;2.

——, L. Mahrt, R. M. Banta, and Y. L. Pichugina, 2012: Turbulence regimes and turbulence intermittency in the stable boundary layer during CASES-99. *J. Atmos. Sci.*, **69**, 338–351, doi:10.1175/JAS-D-11-082.1.

S. J. A. van der Linden, P. Baas, J. A. van Hooft, I. G. S. van Hooijdonk, F. C. Bosveld, and B. J. H. van de Wiel, 2017: Local characteristics of the nocturnal boundary layer in response to external pressure forcing. *J. Appl. Meteor. Climatol.*, doi:10.1175/JAMC-D-17-0011.1, in press.

van de Wiel, B. J. H., R. J. Ronda, A. F. Moene, H. A. R. De Bruin, and A. A. M. Holtslag, 2002: Intermittent turbulence and oscillations in the stable boundary layer over land. Part I: A bulk model. *J. Atmos. Sci.*, **59**, 942–958, doi:10.1175/1520-0469(2002)059<0942:ITAOIT>2.0.CO;2.

——, A. F. Moene, H. J. J. Jonker, P. Baas, S. Basu, J. M. M. Donda, J. Sun, and A. A. M. Holtslag, 2012: The minimum wind speed for sustainable turbulence in the nocturnal boundary layer. *J. Atmos. Sci.*, **69**, 3116–3127, doi:10.1175/JAS-D-12-0107.1.

——, and Coauthors, 2017: Regime transitions in near-surface temperature inversions: A conceptual model. *J. Atmos. Sci.*, **74**, 1057–1073, doi:10.1175/JAS-D-16-0180.1.

van Heerwaarden, C. C., and J. P. Mellado, 2016: Growth and decay of a convective boundary layer over a surface with a constant temperature. *J. Atmos. Sci.*, **73**, 2165–2177, doi:10.1175/JAS-D-15-0315.1.

van Hooijdonk, I. G. S., J. M. M. Donda, H. J. H. Clercx, F. C. Bosveld, and B. J. H. van de Wiel, 2015: Shear capacity as prognostic for nocturnal boundary layer regimes. *J. Atmos. Sci.*, **72**, 1518–1532, doi:10.1175/JAS-D-14-0140.1.

——, A. F. Moene, M. Scheffer, H. J. H. Clercx, and B. J. H. van de Wiel, 2017: Early warning signals for regime transition in the stable boundary layer: A model study. *Bound.-Layer Meteor.*, **162**, 283–306, doi:10.1007/s10546-016-0199-9.

van Meijgaard, E., L. Van Ulft, W. Van de Berg, F. C. Bosveld, B. J. J. M. Van den Hurk, G. Lenderink, and A. P. Siebesma, 2008: The KNMI regional atmospheric climate model RACMO version 2.1. Koninklijk Nederlands Meteorologisch Instituut Tech. Rep. 302, 43 pp., http://bibliotheek.knmi.nl/knmipubTR/TR302.pdf.

van Ulden, A. P., and J. Wieringa, 1996: Atmospheric boundary layer research at Cabauw. *Bound.-Layer Meteor.*, **78**, 39–69, doi:10.1007/BF00122486.

Vignon, E., C. Genthon, H. Barral, C. Amory, G. Picard, H. Gallée, G. Casasanta, and S. Argentini, 2016: Momentum- and heat-flux parametrization at Dome C, Antarctica: A sensitivity study. *Bound.-Layer Meteor.*, **162**, 341–367, doi:10.1007/s10546-016-0192-3.

——, and Coauthors, 2017: Stable boundary layer regimes at Dome C, Antarctica: Observation and analysis. *Quart. J. Roy. Meteor. Soc.*, **143**, 1241–1253, doi:10.1002/qj.2998.

Wauben, W., F. Bosveld, and H. K. Baltink, 2010: Laboratory and field evaluation of the nubiscope. WMO Tech. Doc. 1546, 19 pp., https://www.wmo.int/pages/prog/www/IMOP/publications/IOM-104_TECO-2010/1_7_Waubenetal_Netherlands.pdf.

Whiteman, C. D., T. Haiden, B. Pospichal, S. Eisenbach, and R. Steinacker, 2004: Minimum temperatures, diurnal temperature ranges, and temperature inversions in limestone sinkholes of different sizes and shapes. *J. Appl. Meteor.*, **43**, 1224–1236, doi:10.1175/1520-0450(2004)043<1224:MTDTRA>2.0.CO;2.